THE JOURNAL OF PHYSICAL CHEMISTRY C

Article

pubs.acs.org/JPCC

Ni Substitutional Defects in Bulk and at the (001) Surface of MgO from First-Principles Calculations

Aliaksei Mazheika* and Sergey V. Levchenko

Fritz-Haber-Institut der Max-Planck-Gesellschaft, Faradayweg 4-6, 14195 Berlin, Germany

Supporting Information

ABSTRACT: Electronic and structural properties of nickel substitutional defects in the bulk and at (001) terraces, steps, and corners of magnesium oxide, as well as adsorption of CO, CO_2, CH_4, and H_2 on them, are studied using hybrid density-functional theory, coupled-cluster model with single, double, and perturbative triple substitutions [CCSD(T)], and perturbative *GW* approximation. The amount of exact exchange (α) in the HSE(α) hybrid functional is validated against the higher-level methods. We find that with α = 0.3, formation energies of Ni_{Mg} defects and adsorption energies of CO, CO_2, and H_2 calculated with HSE are close to ones obtained with CCSD(T), whereas for ionization of Ni_{Mg} α = 0.44−0.5 is needed to reproduce G_0W_0@HSE(α) ionization energy. The dependence of the adsorption energies on α is found to be weaker than the dependence of formation and ionization energies: changing α from 0.25 to 0.44 results in variation of adsorption energies on the order of up to 0.2 eV. HSE calculations with the optimal α revealed that Ni_{Mg} is most stable at corner sites on MgO(001), followed by the subsurface, bulk, and step sites, which are very similar in energy (within 0.03 eV), and then the terrace sites (0.45 eV less stable than at corner sites). In the bulk, Ni_{Mg} defects serve as traps for both holes and electrons. The presence of these defects at the MgO surface is found to have a weak effect on energies of CH_4 physisorption and CO_2 chemisorption, whereas it favors chemisorption of CO and dissociation of H_2 and methane.

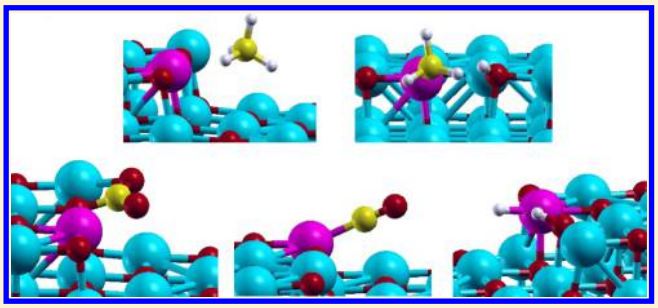

1. INTRODUCTION

Supported metal−nanoparticle catalysts are widely used for environment purification and energy conversion.[1−3] Such catalysts potentially have a great versatility: one can change the type of metal, the type of support, and the size of the nanoparticles. In practice, however, the versatility is strongly reduced because of a limited control over the catalyst properties at realistic conditions: at high temperatures, the metal particles tend to sinter, and the type of metal is limited to precious metals such as Pt and Au due to their stability with respect to poisoning by adsorbates. This inevitably reduces the stability of supported catalysts and increases their cost.

An alternative paradigm for supported catalysts has been suggested recently:[4] instead of trying to stabilize metal nanoparticles at a surface, start from a solid solution of the metal in the support. The formation of solid solution implies atomic dispersion of the catalytically active component in the support and stability with respect to sintering. In the case of an oxide support, this also implies that the metal catalyst is oxidized, which can partially or completely deactivate it. However, the catalyst can be (re)activated by placing it in a reducing atmosphere, and the degree of reduction can be to some extent controlled by the treatment conditions.[5] The partial oxidation can be also beneficial, depending on the reaction. As a result, one ends up with metal species at the surface whose stability with respect to sintering is ensured by their partial dissolution in the support.

The above paradigm has been demonstrated on methane and CO_2 conversion over transition-metal-oxide/MgO solid solutions,[6] in particular NiO/MgO solid solutions. Ni can easily replace Mg in MgO lattice due to close ionic radii of Ni^{2+} and Mg^{2+}. In fact, NiO is soluble in MgO in the whole composition range[9] without significant changes in lattice parameters, as both possess similar crystal structure. NiO/MgO solid solutions have been shown to exhibit very promising catalytic properties (activity, selectivity, *and* stability) for dry reforming of methane,[7] and, at different temperature and pressure conditions, for full CO_2 hydrogenation (Sabatier reaction),[8] which is in fact a great breakthrough, since the catalyst does not contain any precious metals.

However, further development of this catalyst is impeded by its complexity for both atomic-resolution experiments and accurate modeling. It was demonstrated that the activity and selectivity of the NiO/MgO catalyst is strongly affected by the composition and preparation conditions,[5] and that the formation of the solid solution is the key to the enhanced activity and stability.[10] It was also shown by transient isotope

Received: September 21, 2016
Revised: November 3, 2016
Published: November 4, 2016

DOI: 10.1021/acs.jpcc.6b09505
J. Phys. Chem. C 2016, 120, 26934−26944

experiments that the lattice oxygen participates in the reaction between CH_4 and CO_2.[11] However, no reliable information on atomic structure of the catalytic surface, or on the nature of active sites, is available.

Theoretical studies of NiO/MgO solid solutions are scarce, while isolated Ni_{Mg} defects in MgO received substantial attention. Timmer and Borstel[12] used an LMTO Green's-function method and LDA to describe electronic structure of isolated Ni_{Mg} defects in MgO, and Giordano et al. used GGA for the same purpose.[13] They concluded that Ni_{Mg} introduces defect levels of mainly Ni 3*d* character in MgO band gap. Torres and Liu[14] showed using GGA that Ni substitutional defects prefer to be in the bulk or subsurface layers of MgO (001), and that only formation of complexes of oxygen vacancy with strictly one Ni_{Mg} in solid solutions stabilizes Ni_{Mg} defects at the surface. In the case of two or more Ni_{Mg} in the neighborhood of O_{vac}, such effect is not pronounced. Pacchioni et al.[15] showed that the adsorption energy and geometry for CO on Ni_{Mg} defect at MgO(001) are quantitatively close to CO on NiO(001), and, based on the comparison with experimental measurements for the latter system (temperature desorption spectroscopy[16] and scanned-energy mode photoelectron diffraction[17,18]) emphasized the necessity for an accurate account of electronic correlation in both cases for a reliable evaluation of the adsorption energy. Valero et al.[19] presented an in-depth analysis of theoretical results on CO and NO adsorption on a series of cluster and slab models of NiMgO and NiO with a variety of wave function and DFT methods. They revealed a strong effect of the basis set on the calculated adsorption energies, and concluded that none of the explored local, semilocal, and hybrid functionals was able to provide accurate results simultaneously for adsorption geometries, energetics, and vibrational frequency shifts. Thus, electronic and adsorption properties of Ni_{Mg} defects in MgO depend strongly on used computational methods, in particular on chosen density-functional approximation. This indicates that the cancellation of errors in the calculated properties does not occur. In particular, local and semilocal functionals suffer from self-interaction error that leads to electron overdelocalization. The substitution of a fraction α of exchange energy by its exact counterpart in the generalized Kohn−Sham scheme[20] reduces this error. The value of α has a strong influence on calculated properties such as band gap, defect formation energy, adsorption energy, etc.,[21−24] and is traditionally chosen based on comparison of molecular atomization energies calculated with DFT and higher-level methods.[20] However, recent studies indicate that the optimal value of α is system- and property-dependent.[23,24]

In the present work, we explore and apply a different approach[21] to study bulk and surface properties of transition-metal-doped oxides in general, and NiMgO in particular. We first find the optimal α in the HSE hybrid functional by comparing formation and ionization energies for surface and bulk Ni_{Mg} defects in MgO, as well as the adsorption energies of small molecules at the MgO (001) surface with Ni_{Mg}, to CCSD(T) and G_0W_0 calculations. This comparison is done using embedded cluster models. Once the optimal α (possibly different for different properties) is found, we perform hybrid periodic HSE(α) calculations of NiMgO with converged basis set and supercell size. In particular, we calculate adsorption energies of molecules relevant for catalytic methane and CO_2 conversion (CO, CO_2, CH_4, and H_2) at terraces, steps, and corners at the (001) surface of Ni-doped MgO and compare them to previous theoretical studies. We also study formation energies of Ni_{Mg} defects at different surface and subsurface sites at MgO(001), and explore whether the substitutional defects can serve as donors of charge carriers. We have found no published reports of experimental studies on formation energies of Ni_{Mg} defects or adsorption of molecules on them. However, we do compare our calculations for adsorption at MgO surface and at Ni_{Mg} defects with the available experimental results on MgO and NiO.[16−18,45,46,58,59,62]

2. METHODOLOGY

The validation part was done without geometry relaxation within the embedded-cluster approach in which relatively small to middle-size clusters are placed in the field of point charges and pseudopotentials (or effective-core potentials). In such a way, adsorption energies of CO, CO_2, and H_2, as well as formation energies of bulk and surface Ni_{Mg} defects in MgO were calculated at HSE(α) level and compared to CCSD(T). For this reason we used embedded-clusters simulating the terrace-site of the MgO (001) surface: $NiMg_8O_9(PP)_{49}$, monolayer-step $NiMg_8O_9(PP)_{49}$, and Ni_{Mg} bulk $NiMg_{12}O_6(PP)_{50}$ (PP - pseudopotentials) (Figure 1). Lattice

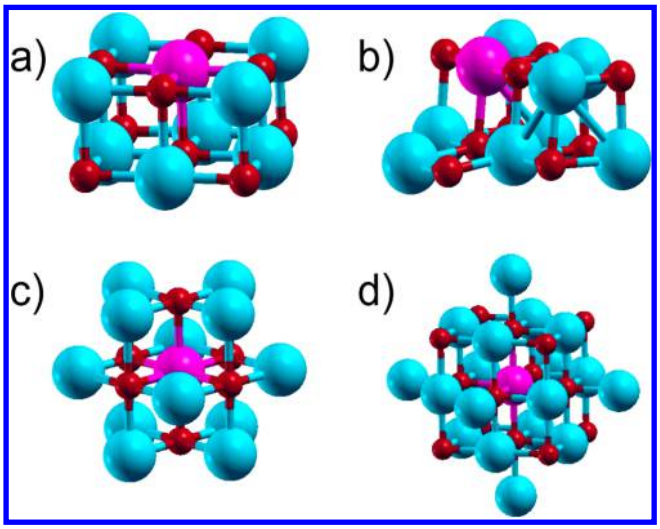

Figure 1. Embedded-cluster models: (a) terrace-site $NiMg_8O_9(PP)_{49}$, (b) monolayer-step $NiMg_8O_9(PP)_{49}$, (c) $NiMg_{12}O_6(PP)_{50}$, (d) $NiMg_{18}O_{14}(PP)_{44}$. Red spheres - O atoms; blue - Mg; purple - Ni. Point charges and PP's are not shown.

parameter of MgO (4.211 Å) and geometry of adsorbed molecules were set to ones obtained in HSE06[25,26] periodic bulk calculations. CCSD(T) and some MP2 calculations were done with the Orca program,[27] whereas HSE and also MP2 were done with FHI-aims.[28] In all cases, the complete basis set (CBS) limit was calculated using two-point extrapolation, so-called focal-point method.[29] For this purpose we used cc-pV*X*Z[30] basis sets in Orca, with X = D, T for coupled-cluster, and T,Q for MP2, and numeric atomic orbitals NAO-VCC-XZ[31] (X = T,Q,5) for MP2 and HSE in FHI-aims. In addition, the calculations within random-phase approximation (RPA) in(ex)cluding renormalized single-excitations (rSE) and second-order screened exchange (SOSEX) have been done with the same settings.

For the validation of HSE ionization energy, vertical ionization potentials (IPs) were calculated using $NiMg_{12}O_6(PP)_{50}$ and $NiMg_{18}O_{14}(PP)_{44}$ embedded-cluster models

DOI: 10.1021/acs.jpcc.6b09505
J. Phys. Chem. C 2016, 120, 26934−26944

of bulk Ni_{Mg}. The HSE(α) results were compared to ones obtained with the perturbative G_0W_0@HSE(α) method. These calculations were performed with FHI-aims, and the same computational settings were used as for adsorption and formation energies. Zeroth-order regular approximation (ZORA)[32] was used to treat relativistic effects unless the comparison between Orca and FHI-aims was done, in which case no relativistic effects were included.

Hybrid periodic calculations were performed with FHI-aims.[33] The number of k-points was set for each particular supercell by scaling down the 8 × 8 × 8 Γ-centered grid used for the cubic 8-atom MgO unit cell. Lattice parameter was the same as in embedded-cluster calculations. We used 'tight' basis sets and numerical settings according to the nomenclature of the FHI-aims code.[28] van der Waals (vdW) forces were calculated with a first-principles many-body-dispersion approach.[34] Counterpoise method for correcting the basis-set superposition error in adsorption energies was used both in embedded-cluster and slab-periodic studies.

The calculations of charged defects were done applying virtual-crystal approximation (VCA).[21,35,36] In our case, the charges of all O-nuclei in the unit cell and the corresponding number of O valence electrons (to keep the unit cell neutral) were adjusted to simulate either *n*- or *p*-type doping. Supercells 2 × 2 × 2, 3 × 3 × 3, and 4 × 4 × 4 obtained from the 8-atom cubic unit cell were used for the VCA formation-energy calculations, and the results were extrapolated to the dilute limit according to the function $a + b/L + c/L^3$ using the least-squares method.

The adsorption energies are calculated according to the equation

$$E_{ads} = E_{molecule@NiMgO} - E_{NiMgO} - E_{molecule,} \quad (1)$$

where $E_{molecule@NiMgO}$ is the total energy (per unit cell in case of periodic calculations) of Ni-doped MgO with adsorbed molecule, E_{NiMgO} is the total energy of NiMgO without the molecule, and $E_{molecule}$ is the total energy of the molecule. Formation energies of defects are estimated as

$$E_f = E_{NiMgO} - E_{MgO} + \mu_{Mg} - \mu_{Ni} + q\mu_e \quad (2)$$

where E_{MgO} is the total energy of the corresponding MgO cluster or unit cell, μ_X are chemical potentials (X = Mg, Ni, or e for electrons), and q is the number of removed electrons.

More computational details can be found in the Supporting Information (SI).

3. RESULTS AND DISCUSSION

3.1. Electronic Structure and Formation Energy of Ni_{Mg} Substitutional Defects in MgO. The 5-fold degenerate 3*d*-shell of a Ni^{2+} ion is split into a 2-fold (e_g symmetry) and a 3-fold (t_{2g} symmetry) degenerate states in an octahedral crystal field (Figure 2). The degenerate e_g orbitals are occupied by one electron each, while the t_{2g} orbitals accommodate six electrons. This simple picture is, however, somewhat misleading in the case of Ni_{Mg} in MgO, because all Ni 3*d* orbitals are strongly mixed with O 2*p* orbitals, with lowest mixing obtained for PBE (α = 0) (Figure 3, inset). The states of mixed 2*p*(O)/3*d*-e_g(Ni) character appear in the gap above the valence-band maximum (VBM), and approach VBM as α is increased. Figure 2 shows the projected density of states for Ni_{Mg}, calculated with HSE06.

Formation energy of an impurity in a host lattice is sensitive to the local atomic environment. Therefore, it can be used as a probe for the accuracy of the DFT functional in describing hybridization and bonding of the impurity atom with the surrounding atoms. Table 1 and Figure 4 (see also Figure S1 in the SI) summarize the results of calculations of Ni_{Mg} formation energies with various methods both in the bulk and at the surface of MgO. Chemical potential references for nickel and magnesium are chosen as total energies of Ni^{2+} and Mg^{2+} ions

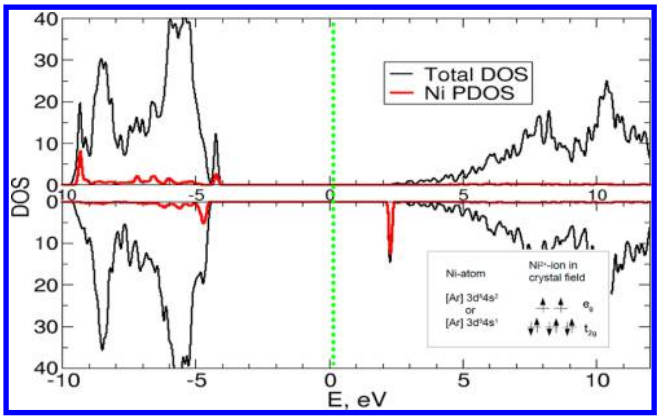

Figure 2. Total and Ni-projected densities of states (in (eV·$V_{unit\ cell}$)$^{-1}$) for Ni-doped MgO calculated with HSE06, *tight*-settings, 2 × 2 × 2 supercell. In the inset, the electronic structure of free Ni-atom and Ni^{2+}-ion in an octahedral crystal field are shown. Energy-zero corresponds to Fermi energy.

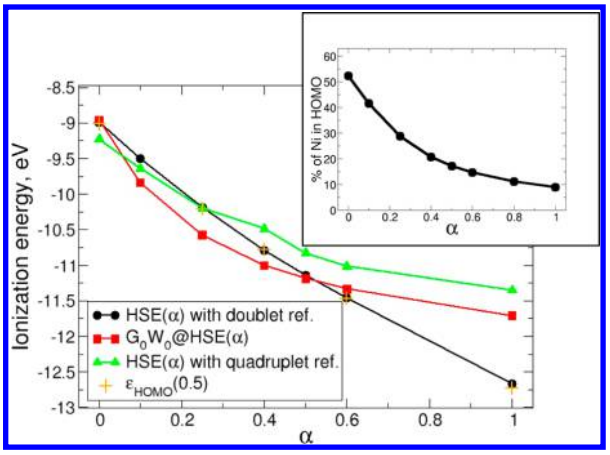

Figure 3. Vertical ionization energies of $NiMg_{18}O_{14}$ embedded cluster calculated with different methods. Inset: the contribution of Ni orbitals to the HOMO of embedded $NiMg_{18}O_{14}$ as a function of α.

Table 1. Adsorption Energies (in eV) of CO at NiMgO and MgO (001) Terrace, CO_2 at a Step at the NiMgO Surface, and Formation Energies of Ni_{Mg} in MgO Calculated Using Embedded Cluster Models As Described in the Text

	CO@ Ni_{Mg}MgO	CO@ MgO	CO_2@ Ni_{Mg}MgO	Ni_{Mg}MgO
HSE(0.25)	−0.49	+0.04	−3.42	−2.27
HSE(0.4)	−0.40	+0.05	−3.65	−1.88
RPA	−0.28	+0.21	−3.24	−1.51
RPA+rSE	−0.92	−0.13	−3.24	−3.09
RPA+rSE +SOSEX	−0.68	−0.10	−3.73	−2.69
MP2	−0.40	+0.06	−3.34	−1.98
CCSD	−0.35	+0.09	−3.55	−1.97
CCSD(T)	−0.44	+0.07	−3.46	−2.20

DOI: 10.1021/acs.jpcc.6b09505
J. Phys. Chem. C 2016, 120, 26934−26944

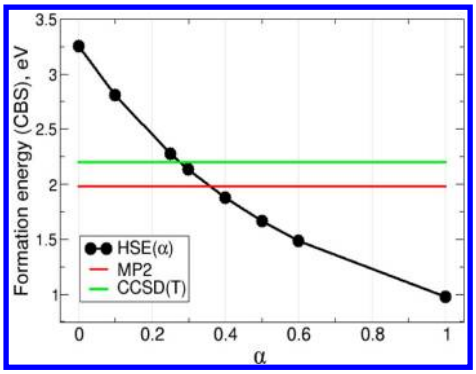

Figure 4. Formation energies of Ni_{Mg} in the bulk obtained with different methods.

in the gas phase, to make CCSD(T) calculations of the formation energies feasible.

The HSE results indeed show a strong dependence on α (Figure 4), reflecting the change in hybridization of Ni and O atoms. The difference between MP2 and CCSD(T) is about 0.23 eV for bulk and 0.05 eV for surface Ni_{Mg} defect, whereas between CCSD and CCSD(T) it is 0.24 and 0.15 eV, respectively. The optimal α is about 0.275−0.28 in both cases, with the CCSD(T) formation energy deviating from the HSE06 value (α = 0.25) by 0.08 eV also in both cases. PBE0 (α = 0.25, ω = 0) yields formation energy of bulk Ni_{Mg} differing from HSE06 by −0.09 eV, indicating a weak dependence on ω for $0 < \omega < 0.11$ $bohr^{-1}$. Increasing the size of the cluster model ($NiMg_{18}O_{14}(PP)_{44}$, Figure 1d) has a minor effect (~0.02 eV) on the formation energy calculated at the HSE(α) level. Moreover, HSE(0.3) gives bulk NiO and MgO cohesive energies (obtained with a periodic model) with respect to free atoms close to a high-level quantum Monte Carlo (QMC) calculations and experimental data: 8.81 versus 9.80 ± 0.85[37] eV for NiO and 9.74 versus 10.45[38] eV for MgO. The same for lattice energies with respect to free ions: 41.3 versus 41.0 ± 0.5[38] eV for NiO and 39.1 versus 39.3[38] eV for MgO.

RPA combined with exact exchange is a promising approach for solid-state calculations. It seamlessly incorporates dispersion interaction, and is computationally feasible even for relatively large unit cell sizes (up to 100 atoms). However, we find that RPA strongly underestimates formation energy of Ni_{Mg} by 0.69 eV. Inclusion of rSE leads to overestimation by 0.89 eV, and addition of SOSEX improves the RPA+rSE result, but the rPT2 value is still 0.49 eV higher than CCSD(T) (Table 1).

Ionization energy is another sensitive probe for the chemical interactions between the impurity and the lattice atoms. It is also a strict test of the accuracy of a DFT approximation, because the difference in energies between different charge states of a system does not benefit from the cancellation of the self-interaction error. We calculate ionization energies using the G_0W_0 approach, because ΔSCF calculations with single-reference MP2 or coupled-cluster methods do not account for static correlation in the ionized system (see SI) in this case. The static correlation can also affect ionization energies calculated with HSE(α) using the ΔSCF approach. However, there are indications that at least part of the static correlation is accounted for by approximate DFT functionals.[39] In addition, one can use the Slater Xα concept,[40,41] in which the ionization energy is calculated as the energy $\varepsilon_{HOMO}(0.5)$ of the highest-occupied orbital (HOMO) at half-occupation. We find that the state with 0.5 electrons removed is nondegenerate, and that $\varepsilon_{HOMO}(0.5)$ coincides with the HSE(α) ΔSCF for all α, indicating that static correlation is accounted for in our DFT approach.

We therefore proceed by calculating HSE(α) ΔSCF and G_0W_0@HSE(α) HOMO energy level and finding the crossing point of the corresponding functions of α, which yields the optimal α for this property.[21] The results for the embedded cluster $NiMg_{18}O_{14}$ are shown in Figure 3. In the SI, similar results for the smaller cluster $NiMg_{12}O_6$ are presented. For both methods, CBS limit is obtained by extrapolating from the NAO-cc-pVTZ and NAO-cc-pVQZ basis sets. The strong dependence of the ionization energy on α reflects the localized nature of the highest occupied state.

We calculate HSE(α) ΔSCF for two spin-states of the ionized system: with S_z = 0.5 and S_z = 1.5 (Figure 3). G_0W_0 shows a strong starting-point dependence at $\alpha < 0.4$, indicating a significant change in character of HOMO. Indeed, the contribution of Ni 3*d* orbitals to HOMO reduces from 50% to 20% as α increases from 0 to 0.5, and then reduces further from 20% to 10% for larger values of α (see inset in Figure 3). The HSE(α) ΔSCF lines corresponding to the two states of the ionized system with different spin-projections follow each other closely for $\alpha \leq 0.6$, reflecting quasi-degeneracy of different electronic configurations. At $\alpha > 0.6$, the ionized state with S_z = 1.5 becomes the ground state; for instance, the difference between doublet and quadruplet for α = 1.0 is 1.32 eV. This happens because introduction of exact exchange decreases self-interaction energy of an electron in e_g-states, and its energy decreases approaching the energy of t_{2g}-level. At $\alpha \approx 0.25$, the transfer of one electron from t_{2g} to e_g occurs following the Hund's rule. With further increase of α the quadruplet state is further stabilized. However, $\varepsilon_{HOMO}(0.5)$ coincides with the S_z = 0.5 line (Figure 3), and this is the line that has a crossing with G_0W_0@HSE(α) HOMO.

The resulting optimal α is 0.44 for the smaller cluster model (see Figure S2 in SI), and around 0.5 for the larger one. Although the G_0W_0 line crosses the HSE one also at α = 0, we do not consider it as optimal value, because at this point other solutions of *GW* equations were found, indicating some uncertainty of this result. A detailed analysis of multiplet solutions to the *GW* quasiparticle equation will be presented elsewhere. The deviation from α = 0.25 is 0.74 and 0.95 eV for $NiMg_{12}O_6$ and $NiMg_{18}O_{14}$, respectively. The difference between α = 0.44 and 0.5 for both clusters is about 0.2 eV. PBE0 ΔSCF ionization energy is lower than the HSE06 one by 0.04 eV. The band gap of MgO is increased by 0.4 eV when α is increased from 0.44 to 0.5, as obtained from periodic calculations.

The method for finding the optimal α is also applied to the difference between ionization energies of the cluster with Ni and the same cluster with Ni replaced by Mg. This property describes charging of Ni_{Mg} in *p*-doped MgO by trapping holes. The resulting optimal α is 0.49, which is close to the optimal α for ionization energy with respect to vacuum.

Thus, we obtain a different optimal α for ionization energy versus the formation energy. In view of the challenges in *GW* calculations for systems with multiplet solutions, this result requires further investigation. Nevertheless, below we use the optimal α = 0.5 obtained for the ionization energy to describe charging of the NiM_g impurities in bulk MgO. For neutral impurities α = 0.3 is used.

We now apply HSE(α) combined with many-body dispersion[34] to calculate formation energies of Ni_{Mg} defects

DOI: 10.1021/acs.jpcc.6b09505
J. Phys. Chem. C 2016, 120, 26934−26944

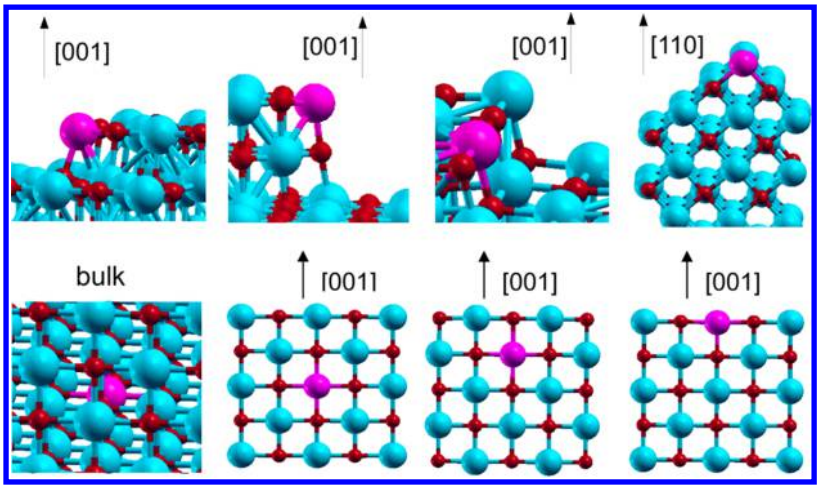

Figure 5. Ni_{Mg} defects at the (001) surface and in the bulk of MgO; upper row (left to right): monolayer-corner, two-layer corner, monolayer-step, "edge"-site; bottom row (left to right): bulk, Ni_{Mg} at the third subsurface layer, at the second layer, at the terrace-site. Red spheres represent O atoms, blue - Mg, and purple - Ni.

Table 2. Formation Energies of Ni_{Mg} Defects Calculated with Periodic Models[a]

site	bulk	terrace	second layer	3d layer	monolayer step	"edge"-site	corner at monolayer	corner at bilayer
E_f, eV	−2.53	−2.46	−2.54	−2.51	−2.53	−2.48	−2.91	−2.81

[a]The method is HSE(0.3)+vdW with *tight* settings.

using periodic models. Ni_{Mg} defects at sites with different coordination are considered: in the bulk, at the (001) terrace, in the second and third subsurface layers of MgO(001), at an "edge"-site (see Figure 5, upper row, right), at the monolayer step of MgO(001), and at the Mg-corner formed by monolayer or bilayer steps. The "edge" was modeled as a slab of (110) surface with added rows of atoms. The distance between periodically replicated Ni-atoms was 8.42 Å along the edge and 8.93 Å in perpendicular direction. The monolayer step was modeled as a 5-atomic-layer 2 × 3 or 2 × 4 (001) slab with 2 or 4 atomic rows removed from the top layer, respectively. The corner-site was simulated with a 3-atomic-layer slab with 16- or 25-atomic monolayer 0D "island" of the square shape. In case of the corner of bilayer-step additional layer of the same lateral dimensions was added to the "island".

Formation energies calculated according to eq 2 are summarized in Table 2. The chemical potentials of Ni and Mg are set to the energy of Ni^{2+} and Mg^{2+} ions in the gas phase, respectively, in the same way as it was done for validation of theory level. We find that the Mg-corner site is the most favorable one for Ni_{Mg}. Formation energies at the other sites are very similar to each other. The lowest formation energy is obtained for the terrace site which is by about 0.07 eV lower than in the bulk. Starting from the second monolayer and further toward the bulk, Ni_{Mg} formation energies almost do not change. Increasing the height of corner/step decreases the formation energy by 0.10/0.05 eV. van der Waals interaction increases the absolute value of formation energy by 0.15 eV for bulk, 0.09 eV for terrace, 0.06 eV for monolayer step, and 0.05 eV for corner Ni_{Mg}. Our finding that Ni_{Mg} prefers to be in the bulk or in subsurface layers rather than at the (001) terrace qualitatively agrees with the GGA results presented in ref 14.

We have also performed HSE(0.3) calculations of 64-atomic unembedded clusters $NiMg_{31}O_{32}$ with full relaxation and *tight*-settings, to investigate the size effect on Ni_{Mg} defects. The pristine $Mg_{32}O_{32}$ has a cubic shape in the gas phase. Ni_{Mg} was placed at the face, inside, at the edge, and at the Mg-corner of the cube. Relative energies of relaxed clusters show that the most stable position of Ni_{Mg} is still at the corner site, then follows the structure with Ni_{Mg} inside the cube (energy is higher by 0.18 eV), then Ni_{Mg} at the edge (+0.22 eV) and finally the structure with Ni_{Mg} at the surface (+0.25 eV). Compared to the extended surface, the general trend is the same, although the differences in formation energies between corner and other sites are slightly different.

Formation of a neutral oxygen vacancy (F^0 center) near the Ni_{Mg} defect in the bulk with was also calculated with HSE(0.3) according to

$$E_f = E_{vac} + \mu_O - E_{host} \quad (3)$$

where E_{vac} and E_{host} are the total DFT energies of the system with and without O vacancy, $\mu_O = E_O(\mathrm{HSE}(0.3)) - 0.5E_{bind}(O_2)$, with the binding energy of O_2, $E_{bind}(O_2)$, calculated with HSE(0.3). The resulting vacancy formation energy is 6.68 eV. It is lower than the HSE(0.3) F^0 formation energy in the pure bulk MgO (7.2 eV). The HSE(0.3) value of $E_{bind}(O_2)$ is higher by about 0.2 eV compared to experimental $E_{bind}(O_2)$.[21] The obtained formation energy implies that oxygen vacancies prefer to be near nickel substitutional atoms. A qualitatively similar result was obtained in ref 14.

To study the formation of ionized Ni_{Mg} in the bulk MgO, we use the HSE(0.5) functional. Formation of species with a trapped hole $(Ni_{Mg})^+$ and with a trapped electron $(Ni_{Mg})^-$ is considered by calculating IP and electron affinity (EA), respectively. For both ionized states, the $O_h \rightarrow D_{4h}$ Jahn–Teller distortion is found. With the lattice parameter 2.11 Å, the lengths of four planar bonds around $(Ni_{Mg})^+$ are 1.93 Å, and the lengths of two axial bonds are 2.12 Å. Distortion around $(Ni_{Mg})^-$ has the same symmetry, with four Ni–O bond distances of 2.25 Å and two bond distances of 2.17 Å.

In the case of a trapped hole, the electron chemical potential is set to VBM, while the energy of trapping electron is

DOI: 10.1021/acs.jpcc.6b09505
J. Phys. Chem. C 2016, 120, 26934–26944

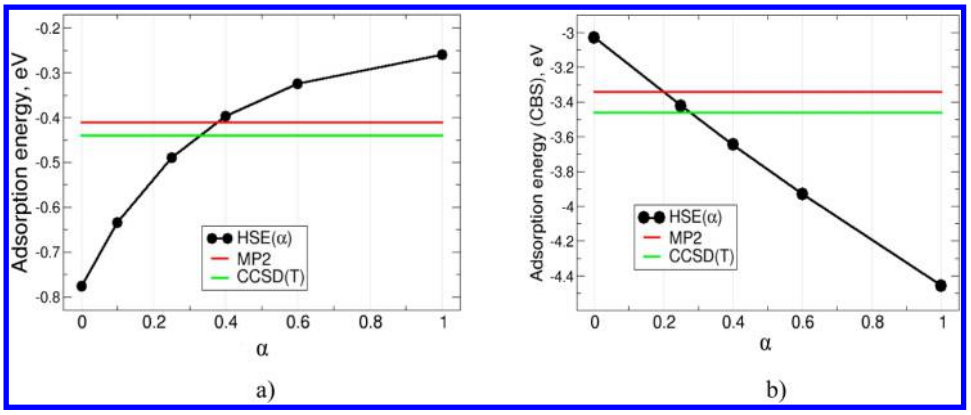

Figure 6. Adsorption energies of CO (a) and CO_2 (b) at NiMgO embedded clusters calculated with different methods.

calculated for μ_e at conduction-band minimum (CBm). In order to find the formation energies in the dilute limit, the results for supercell sizes 2 × 2 × 2, 3 × 3 × 3, and 4 × 4 × 4 are extrapolated as described in Section 2.

We find that the formation energy (relative to the neutral defect, i.e., ionization plus relaxation energy) of $(Ni_{Mg})^+$ calculated with HSE(0.5) is −1.05 eV. In the case of $(Ni_{Mg})^-$, the corresponding value is −1.15 eV. These results show that Ni_{Mg} defects are deep traps for both types of charge carriers.

3.2. Adsorption of CH_4, CO_2, CO, and H_2 at MgO and Ni-doped MgO surfaces. Since adsorption energy is a difference between total energies of similar systems, it is expected that the dependence on α of HSE(α) adsorption energies will be weaker. However, this assumes that the self-interaction error is canceled, which may not be the case when there is a charge transfer between the molecule and the surface. Therefore, we also search for optimal α to describe adsorption energies for the system at hand, and to explore its dependence on the molecular species and surface site coordination. The CCSD(T) calculations are performed for CO, CO_2, and H_2 adsorption using the embedded cluster models with $NiMg_8O_9$ stoichiometry (Figure 1a,b). The difference between MP2 and CCSD(T) adsorption energies obtained with DZ and TZ-quality settings (E_{ads}(CCSD(T)) − E_{ads}(MP2)) is found to be in the range 0.04−0.13 eV depending on the adsorbate. For CO@NiMgO, this small difference (40 meV) is consistent with previous calculations.[42] For the CO_2@NiMgO step, the corresponding value is 0.12 eV. The differences between CCSD and CCSD(T) adsorption energies obtained with the same settings are 90 meV for adsorbed CO, 90 meV for CO_2 and 29 meV for H_2. HSE(α) with α = 0.25−0.4 reproduces the CBS limit (obtained with the focal-point approximation) of CCSD(T) CO adsorption energy (see Figure 6a) within 0.09 eV (crossing at α = 0.33). For CO_2 α = 0.25−0.4 was found to reproduce the CCSD(T) adsorption energy within 0.22 eV (crossing at α = 0.28) (Figure 6b). In the case of dissociative H_2 adsorption, we have found that the HSE adsorption energy depends rather weakly on α. Although it does not cross the CCSD(T) line, the maximum difference between HSE(0.3−0.5) and coupled-cluster value is about 0.12 eV. The difference in adsorption energies obtained with HSE06 and HSE(0.33) is about 0.05 eV for adsorbed CO, 0.04 eV for CO_2, and 0.01 eV for H_2. Change of the screening parameter ω to 0 for α = 0.25 (PBE0 functional) results in a small change in adsorption energy (by 0.02 eV for NAO-VCC-QZ basis set) in the case of CO adsorption. The dependence of the optimal α on cluster size was also tested, and was found to be insignificant (see SI).

As can be seen from Figure 6, the dependence of the CO and CO_2 adsorption energies on α is qualitatively different. This difference is explained by the different nature of bonding for the two species at the surface. The binding of CO is partly due to the donation of Ni *d*-electrons to the molecule (see Section 3.1), while CO_2 prefers to bind to an O anion and form CO_3^{2-} species at the surface. Increasing α in HSE(α) leads to an increase in the iconicity of metal−O bonds (confirmed by Hirshfeld analysis) and a stronger localization of Ni *d*-electrons. On one hand, this results in a smaller donation of electrons from Ni to CO and weakening of the CO-surface bond. On the other hand, accumulation of electrons at O anions at the surface leads to a larger electron population on CO_3^{2-}, which stabilizes these species. This is consistent with the fact that binding of CO_2 to the more basic CaO(001) surface is stronger than that to MgO(001).[43]

Table 1 summarizes the results on adsorption energies calculated using embedded-cluster models. RPA, RPA+rSE, and rPT2 (RPA+rSE+SOSEX)[44] results are also listed. RPA is known to generally underestimate binding energies.[44] Inclusion of rSE does not influence CO_2 adsorption, but leads to overestimation of CO adsorption energy. SOSEX on top of RPA+rSE overestimates adsorption energies in all considered systems. More general discussion can be found in the SI.

The obtained results show that the adsorption energies are indeed less sensitive to α for considered molecules, and that the HSE(0.3) provides a good accuracy across different molecules and adsorption sites. We therefore proceed using HSE(0.3)+vdW for calculating adsorption energies using periodic models.

3.2.1. CH_4 Adsorption. Methane adsorbs weakly on bare MgO(001) terrace. Such adsorption was previously extensively studied both experimentally[45,46] and theoretically.[47−50] The estimated value of desorption energy at 0 K without the zero-point vibrational energy contribution is about −0.15 eV, as follows from thermo-programmed desorption (TPD) experiments.[45] Most recent theoretical calculations done with an embedded-cluster model and CCSD(T) yield −0.14 eV.[47] With our periodic slab model and HSE(0.3)+vdW calculations, we obtain adsorption energy of −0.12 eV. Methane prefers a so-called 'dipod' position over the surface, with the distance between the C atom and the nearest Mg atom being 2.97 Å. The many-body van der Waals correction is about 0.09 eV.

When Ni_{Mg} is placed in the first, second, or third layer of MgO(001), the HSE(0.3)+vdW adsorption energies are −0.10,

DOI: 10.1021/acs.jpcc.6b09505
J. Phys. Chem. C 2016, 120, 26934−26944

Table 3. Adsorption Energies (in eV) Corresponding to the Most Stable Structures of CH_4, CO_2, CO, and H_2 on Pristine MgO(001) Terraces and under-Coordinated Sites, and in the Presence of One Ni_{Mg} Atom[a]

	CH_4		CO_2		CO		H_2	
	NiMgO	MgO	NiMgO	MgO	NiMgO	MgO	NiMgO	MgO
terrace	−0.10	−0.12	−0.64	−0.64	−0.37	−0.25	+1.13	+1.78
step	−0.21(−0.29)	−0.27(+0.10)	−2.27	−2.54	−0.62	−0.48	−1.02	−0.53
corner	−0.23	−0.39	−1.66	−2.07	−0.69	−0.59	−0.87	−0.50

[a]The energies for dissociative adsorption of methane are shown in parentheses.

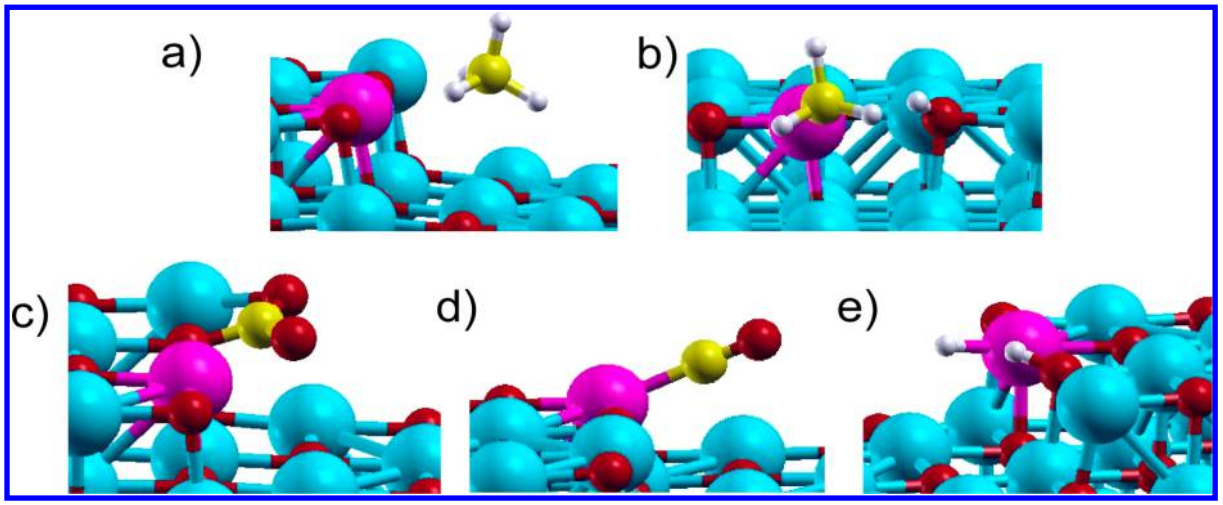

Figure 7. Most stable adsorption structures on NiMgO of CH_4: (a) nondissociative and (b) dissociative; (c) CO_2; (d) CO; (e) H_2. Blue balls − Mg; red − O; yellow − C; white − H; purple − Ni.

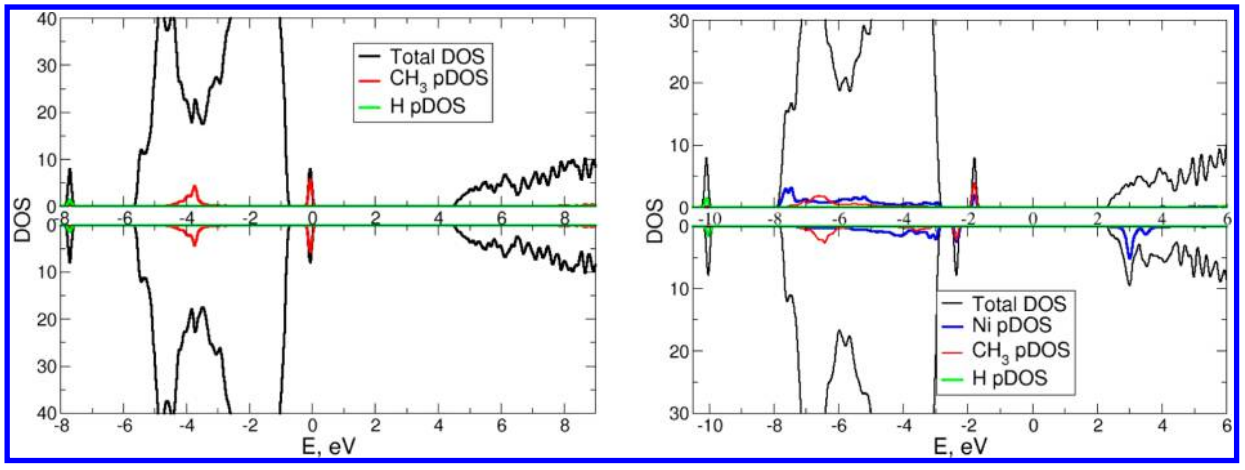

Figure 8. Total density of states (DOS) and projected DOS (in $(eV \cdot V_{unit\ cell})^{-1}$) of dissociated CH_4 on the step of pristine MgO (left) and on the step of MgO with Ni_{Mg} defect (right). Zero on the energy axis corresponds to the position of the Fermi level.

−0.12, and −0.13 eV, respectively. In all cases, the dispersion correction is again about 0.09 eV. The distance between the C atom and surface Ni is 3.08 Å, between C and Mg (if Ni is in the second or third layer) atoms is 2.96 Å, close to the value for CH_4 at pristine MgO(001) terrace. Larger distance and smaller binding energy in the case of Ni_{Mg} in the terrace site is due to increased Pauli repulsion.

Adsorption of CH_4 molecule at under-coordinated sites at pristine MgO surface is more favorable. The adsorption energy is −0.27 eV, if the molecule is at the monolayer step site, and it is −0.39 eV for CH_4 adsorbed at the terrace near the monolayer Mg-corner (Table 3). The distances between C and the nearest Mg of the monolayer step or corner are 2.77 and 2.53 Å, respectively. Our results qualitatively support previous GGA and B3LYP calculations.[49,51]

Introducing Ni_{Mg} substitutional defect slightly decreases the adsorption energies: by 0.06 eV near the step (Figure 7a) and by 0.16 eV near the corner site. van der Waals interaction contributes about 0.14 eV to the energy. The corresponding Ni−C distances are 2.78 Å (step) and 3.15 Å (corner). Compared to MgO, the increase in adsorption energies at step and corner relative to the terrace of Ni-doped MgO is less pronounced (Table 3).

It is well-known that methane can dissociate upon adsorption at low-coordinated Mg and O atoms of MgO.[52] For comparison, we report our HSE(0.3)+vdW results also for this case. The CH_4 molecule breaks to H^+, which binds to the

DOI: 10.1021/acs.jpcc.6b09505
J. Phys. Chem. C 2016, 120, 26934−26944

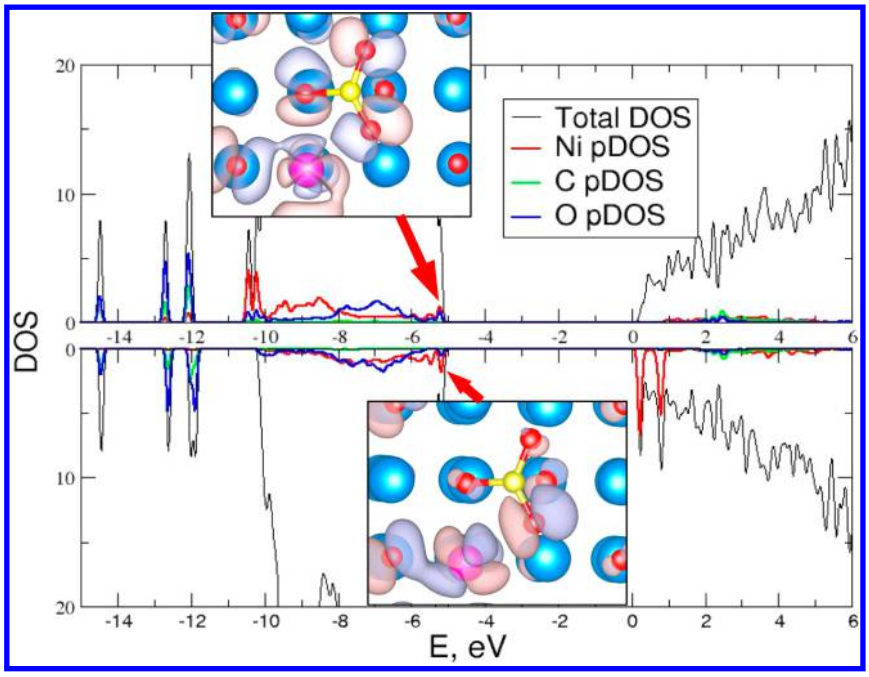

Figure 9. Total density of states (DOS) and projected DOS (in $(eV \cdot V_{unit\ cell})^{-1}$) for carbon dioxide adsorbed at the monolayer step of MgO with Ni_{Mg}. Spin-majority DOS is shown at the top panel, and spin-minority at the bottom. The insets show wave functions for the highest-occupied levels in both spin-channels; blue balls − Mg, red − O, yellow − C, purple − Ni. Zero on the energy axis corresponds to the position of the Fermi level.

O anion, and anionic CH_3^- bonds to the Mg cation.[51,52] We considered such dissociative adsorption at the step site. Our calculations for the pristine MgO show that such process is endothermic with $\Delta_r E$ = +0.10 eV, the equilibrium C−Mg and O−H distances are 2.19 and 0.97 Å, respectively. In the case of Ni_{Mg} at the step (Figure 7b), the dissociative adsorption becomes exothermic, with energy −0.29 eV. This is in contrast to Ni at the surface of CeO_2, where CH_4 dissociation remains endothermic according to DFT+*U* calculations.[53] The C−Ni bond length is shorter (2.02 Å), the O−H bond length is almost the same. The reason for this significant increase in the dissociative adsorption energy is that on the (001) step edge of MgO, the lone pair of the adsorbed CH_3^- (Figure 8, left) is energetically close to the Ni-induced states in the gap (Figure 2), so that the two unpaired electrons in the gap states interact with the CH_3 lone pair (Figure 8, right), increasing the binding energy by 0.4 eV.

Thus, in the case of physisorption, there is no significant difference between CH_4 on pure MgO(001) terrace, on the same surface with Ni_{Mg} at first layer, or with Ni_{Mg} in subsurface layers. In the case of steps and corners, the CH_4 binding to NiMgO is weaker compared to pure MgO, especially for corner. Only in the case of dissociative adsorption of CH_4, the presence of Ni-doping plays a significant role, substantially increasing adsorption energies.

3.2.2. CO_2 Adsorption. The adsorption of carbon dioxide at pristine MgO proceeds with significant change of the geometry. Adsorbed CO_2 forms carbonate-like (CO_3^{2-}) species with a surface O, with O−C−O angle of adsorbed molecule ∼130−133° (Figure 7c). In previous works on CO_2 adsorption at different sites on pristine MgO surface it was found that the adsorption at the monolayer step is strongly favored compared to the terrace.[43,54,55] The exact value of the adsorption energy strongly depends on the computational method. For instance, for the binding energy with terrace site, a wide range of values was obtained, from +0.62 eV to −0.68 eV.[56] Positive energy (meaning endothermic adsorption) was obtained in the embedded-cluster model with B3LYP functional and Gaussian basis sets, + 0.13 eV,[43] although another, more sophisticated embedded-cluster calculation with the same functional and basis sets of TZ- and QZ-quality yielded −0.68 eV.[56] Slab periodic calculations with GGA, plane waves and projector augmented waves (PAW) yield $E_{ads} \approx -0.1$ eV,[54] whereas periodic calculations with B3LYP and basis sets of DZ-quality give −0.38 eV.[57] In all of these DFT studies, van der Waals forces were not included. Experimental study done in early 90-s using TPD suggested that adsorption of CO_2 at the terrace of MgO(001) is indeed exothermic with the energy −0.41 eV.[58]

Our results for adsorption at undercoordinated sites on pristine MgO(001) are −0.64 eV for the terrace site, −2.54 eV at the monolayer step, and −2.07 eV near the Mg corner of a monolayer step (Table 3). Inclusion of exact exchange was found to play a significant role. Our PBE adsorption energy is close to the value reported in ref 54, −0.14 eV. Inclusion of many-body dispersion doubles the PBE adsorption energy to −0.29 eV. In the case of HSE(0.3)+vdW, dispersion contribution is about the same (−0.13 eV), but the overall adsorption energy is −0.64 eV, i.e., twice the PBE+vdW value. Besides the exchange-correlation functional, the quality of basis sets evidently plays a significant role. In our calculations with the *light* set of basis functions instead of *tight*,[28] the binding energy −0.51 eV is obtained. After subtracting from this value the dispersion interaction correction (−0.14 eV), we obtain −0.37 eV, the same value as in the ref 57.

The presence of Ni does not affect the adsorption energies noticeably. For the terrace site containing Ni_{Mg}, the adsorption energy is almost exactly the same (−0.64 eV); at the step, CO_2 binds with an O atom adjacent to Ni_{Mg} with lower energy (−2.27 eV) compared to pure MgO (Table 3); near the Ni-corner the adsorption energy is again lower in absolute value (−1.66 eV). The decrease in adsorption energy is explained by occupation of the antibonding orbitals of CO_3^{2-} by Ni 3*d*

DOI: 10.1021/acs.jpcc.6b09505
J. Phys. Chem. C 2016, 120, 26934−26944

electrons, and the antibonding character of the resulting states, as can be seen in Figure 9. It also results that CO_2 is tilted in opposite direction from Ni by 2.3°. The absence of such antibonding interaction in the case of pristine MgO allows for the stronger binding. At the terrace the overlap of CO_2 and Ni-orbitals is small, and the electrostatic interaction dominates.

3.2.3. CO Adsorption. Carbon monoxide is only weakly adsorbed on pristine MgO with C atom downward, on top of Mg. Previously calculated binding energies for terrace site significantly differ from each other depending on the used method.[59] The most recent calculations done with the method of local-increments yields −0.124 eV,[60] although a combined MP2-CCSD(T) approach gave −0.22 ± 0.01 eV.[61] The experimental adsorption energy derived from thermo-desorption spectroscopy is −0.14 eV[59] or −0.18 ± 0.02 eV.[61] More recent TPD experiments provided a bit higher adsorption energy for the coverage θ = 1/8, −0.21 ± 0.02 eV.[61,62] The HSE(0.3)+vdW calculated value for the same coverage is −0.25 eV (Table 3). Such relatively small binding energy suggests that the adsorption is mainly due to dispersion and electrostatic interaction.

CO is known to interact with compounds containing Ni^{2+}, in particular with NiO, through the so-called Blyholder mechanism: donation of Ni *d*-electrons to CO π^*-orbital, and partial donation of CO σ-electrons to empty Ni 4*s*-orbital.[59,63] $Ni_{Mg}MgO$ behaves similarly in the case of CO-adsorption.[15] The adsorption energy at the terrace site is −0.37 eV, at the monolayer step it is −0.62 eV, and at the corner −0.69 eV (Figure 7d, Table 3). The dispersion interaction contribution is about 0.1 eV for all sites. With decreasing coordination of Ni the binding energy increases, which is explained by the decrease of electronic density on Ni with the decrease in coordination number (terrace > step > corner); corresponding Hirshfeld charges are +0.36, + 0.40, + 0.41. This results in the increase of electronic density donation from CO σ-orbital to Ni ion. The C−O bond length changes very little (1.123 Å, 1.122 Å, and 1.121 Å for the terrace, step, and corner, respectively).

The difference between adsorption energies calculated with the embedded-cluster model (−0.44 eV) and the slab-periodic model (−0.37 eV) is due to the small cluster size. Increasing the number of atoms in the embedded cluster from 18 to 60 ($NiMg_{29}O_{30}$) leads to a decrease in adsorption energy by −0.07 eV, which is already very close to the value from the slab-periodic model. This size effect reflects the degree of delocalization of Ni-induced states.

3.2.4. H_2 Adsorption. Hydrogen prefers to dissociate upon adsorption on MgO. The dissociation is heterolytic.[64−66] Homolytic dissociation is possible under irradiation or on MgO(111) surface.[67] During heterolytic adsorption the positively charged H atom forms an OH group with the underlying surface O atom, while the negatively charged H atom binds with the underlying magnesium atom and forms Mg−H^-. The reaction proceeds both at the (001) terrace of MgO and at the step. At the terrace, the distance between H atoms should be at least 4.7 Å, otherwise they will tend to associate and desorb.[67] In the case of step-adsorption, H atoms bind with neighboring Mg and O atoms of the edge. This reaction proceeds with no barrier.[64−66]

In this work, we consider heterolytic dissociation of hydrogen at (001) terrace, step, and corner of pristine and Ni-doped MgO. For pristine MgO we obtain the following HSE(0.3)+vdW adsorption energies: at terrace site +1.78 eV, at the step −0.53 eV, and −0.50 eV at the Mg-corner. The Mg−H distances are 1.80, 1.83, and 1.77 Å for terrace, step, and corner, respectively, and corresponding O−H bond lengths are 0.96−0.97 Å. These data agree with previous reports.[67] Replacement of Mg by Ni results in an increase of H_2 dissociative adsorption energies, which become +1.13 eV for terrace site, −1.02 eV for step (Figure 7e), and −0.87 eV for corner. At the step and corner with Ni_{Mg} molecular hydrogen also dissociates without a barrier (H_2 molecule dissociates in the course of a geometry relaxation). The O−H distances are the same (~0.96 Å) as for pristine MgO, but Ni−H distances (1.58 Å for terrace site, 1.61 Å for step, and 1.57 Å for corner) are shorter than Mg−H. This implies that a stronger bond is formed between H^- and Ni cation compared to Mg cation. The reason for this stronger binding is similar to the case of dissociative CH_4 adsorption (Figure 8), namely, the overlap of the 3*d*-derived e_g-orbitals of Ni^{2+} with the doubly occupied H *s*-orbital, which is also located near the top of VBM. In the case of pristine MgO, this *s*-orbital can only interact with Mg 3*s*-orbitals, which are much higher in energy, so that the interaction between H^- and the surface remains mainly electrostatic.

4. CONCLUSIONS

The comparison of HSE(α) calculations with CCSD(T) and G_0W_0@HSE(α) results for the same cluster models showed that accurate description of different properties of Ni-doped MgO requires, as might be expected, different fractions of exact exchange α. While the adsorption of small molecules and formation energies of Ni_{Mg} are well described by the HSE functional with $\alpha \approx 0.3$, larger α (0.44−0.5) is required for ionization energies of Ni_{Mg}. We find that, on one hand, the adsorption energies are less sensitive to α: they change by less than 0.3 eV for α increasing from 0.3 to 0.5. On the other hand, both the Ni_{Mg} formation energy and the ionization energy are more sensitive: the formation energy changes by 0.4−0.5 eV and the ionization energy changes by 0.6 eV as α is increased from 0.3 to 0.5. Probable compromise (α close to 0.4) would result in following maximum differences with respect to optimal α for each property: 0.2 eV for adsorption, 0.3 eV for formation, and about 0.2 eV or less for ionization energies.

Using HSE(α) with α = 0.44 or 0.55, we show that Ni_{Mg} defects in the bulk of MgO are deep traps for both electrons and holes. The calculated trapping energies are of the order of 1 eV. This implies that an increase in conductivity of NiO/MgO solid solutions at low Ni content cannot be attributed to Ni_{Mg} defects, but can only be explained by formation of defect complexes.

The relative formation energies of Ni_{Mg} defects at the terrace, subsurface, step, and corner sites at the MgO(001) surface calculated with the HSE(0.3)+vdW functional reveal that the substitutional defects prefer to occupy Mg-corner sites. The step, subsurface, and bulk sites are less favorable, with very small differences in preference for Ni_{Mg} formation among them. The least preferred site is at the terrace, where Ni_{Mg} is by 0.07 eV less stable than in the bulk.

HSE(α)+vdW with α optimal for adsorption energy calculations (α = 0.3) reproduces well the results of previous accurate calculations for CH_4, CO, and CO_2 adsorption (−0.14 eV[47], −0.22 eV,[61] −0.68 eV[56]) on the flat terraces and at under-coordinated sites (step edges and corners) on MgO(001) surface. Introducing Ni_{Mg} defects has a minor effect on adsorption of CH_4 and CO_2 at the terrace, while at step edge and especially corner the adsorption energy of CO_2 is reduced (by 0.27 eV at steps and by 0.41 eV at corners), and CH_4

DOI: 10.1021/acs.jpcc.6b09505
J. Phys. Chem. C 2016, 120, 26934−26944

dissociative adsorption at a step edge with Ni_{Mg} becomes competitive with physisorption, in striking difference to pristine MgO. The dissociative adsorption of H_2 is found to be endothermic on both pristine and Ni-doped terrace MgO(001). However, at steps, Ni_{Mg} defects increase the H_2 dissociative adsorption energy by about 0.5 eV, making it much more favorable than at the steps on pristine MgO surface.

The result that a different optimal α is obtained for ionization energies versus adsorption and formation energies requires further investigation, and will be discussed in detail in a subsequent publication. The multireference character of the ionized states of Ni_{Mg}, originating from low-energy electronic configurations involving excitations from the valence band to the defect level, prevented us from using the standard single-reference coupled-cluster method for calculation of the ionization energies. Multireference methods, or excited-state methods based on the neutral reference (such as equation-of-motion coupled-cluster method for ionization potentials or electron affinities, EOM-CC-IP and EOM-CC-EA) could solve this problem in principle, and would allow one to benchmark the *GW* method for this kind of systems as well. However, at this time there is no implementation available (to our best knowledge) that would allow such calculations for the systems of the size needed for these studies.

■ ASSOCIATED CONTENT

Supporting Information

The Supporting Information is available free of charge on the ACS Publications website at DOI: 10.1021/acs.jpcc.6b09505.

Extensive description of computational details, influence of random-phase approximation (RPA) and beyond RPA on adsorption, and validation of ionization potentials (PDF)

■ AUTHOR INFORMATION

Corresponding Author

*E-mail: mazheika@fhi-berlin.mpg.de; alex.mazheika@gmail.com.

ORCID

Aliaksei Mazheika: 0000-0002-4705-1804

Notes

The authors declare no competing financial interest.

■ ACKNOWLEDGMENTS

The authors are grateful for the financial support from DFG cluster of excellence "Unifying concepts in catalysis" (UniCat). This work greatly benefited from discussions with Matthias Scheffler.

■ REFERENCES

(1) Liu, Y.; Dai, H.; Deng, J.; Xie, S.; Yang, H.; Tan, W.; Han, W.; Jiang, Y.; Guo, G. Mesoporous Co_3O_4-Supported Gold Nanocatalysts: Highly Active for the Oxidation of Carbon Monoxide, Benzene, Toluene, and *o*-Xylene. *J. Catal.* **2014**, *309*, 408−418.

(2) Sedjame, H.-J.; Fontaine, C.; Lafaye, G.; Barbier, J., Jr. On the Promoting Effect of the Addition of Ceria to Platinum Based Alumina Catalysts for VOCs Oxidation. *Appl. Catal., B* **2014**, *144*, 233−242.

(3) Rooke, J. C.; Barakat, T.; Franco Finol, M.; Billemont, P.; De Weireld, G.; Li, Y.; Cousin, R.; Giraudon, J.-M.; Siffert, S.; Lamonier, J.-F.; et al. Influence of Hierarchically Porous Niobium Doped TiO_2 Supports in the Total Catalytic Oxidation of Model VOCs over Noble Metal Nanoparticles. *Appl. Catal., B* **2013**, *142*−*143*, 149−160.

(4) Xia, Y.; Xiong, Y.; Lim, B.; Skrabalak, S. E. Shape-Controlled Synthesis of Metal Nanocrystals: Simple Chemistry Meets Complex Physics. *Angew. Chem., Int. Ed.* **2009**, *48*, 60−103.

(5) Ruckenstein, E.; Hu, Y. H. The Effect of Precursor and Preparation Conditions of MgO on the CO_2 Reforming of CH_4 over NiO/MgO Catalysts. *Appl. Catal., A* **1997**, *154*, 185−205.

(6) Ruckenstein, E.; Hu, Y. H. Binary MgO-based Solid Solution Catalysts for Methane to Syngas. *Catal. Rev.: Sci. Eng.* **2002**, *44*, 423−453.

(7) Choudhary, V. R.; Uphade, B. S.; Mamman, A. S. Simultaneous Steam and CO_2 Reforming of Methane to Syngas over NiO/MgO/SA-5205 in Presence and Absence of Oxygen. *Appl. Catal., A* **1998**, *168*, 33−46.

(8) Nakayama, T.; Ichikuni, N.; Sato, S.; Nozaki, F. Ni/MgO Catalyst Prepared Using Citric Acid for Hydrogenation of Carbon Dioxide. *Appl. Catal., A* **1997**, *158*, 185−199.

(9) Yoshida, T.; Tanaka, T.; Yoshida, H.; Funabiki, T.; Yoshida, S. Study on the Dispersion of Nickel Ions in the NiO-MgO System by X-ray Absorption Fine Structure. *J. Phys. Chem.* **1996**, *100*, 2302−2309.

(10) Ruckenstein, E.; Hu, Y. H. Methane Partial Oxidation over NiO/MgO Solid Solution Catalysts. *Appl. Catal., A* **1999**, *183*, 85−92.

(11) Ruckenstein, E.; Hu, Y. H. Role of Lattice Oxygen During CO_2 Reforming of Methane over NiO/MgO Solid Solutions. *Catal. Lett.* **1998**, *51*, 183−185.

(12) Timmer, G.; Borstel, G. Electronic Structure of Nickel, Iron, and Cobalt Impurities in Magnesium Oxide. *Phys. Rev. B: Condens. Matter Mater. Phys.* **1991**, *43*, 5098−5108.

(13) Prada, S.; Giordano, L.; Pacchioni, G. Li, Al, and Ni Substitutional Doping in MgO Ultrathin Films on Metals: Work Function Tuning via Charge Compensation. *J. Phys. Chem. C* **2012**, *116*, 5781−5786.

(14) Torres, D.; Liu, P. Vacancy-Driven Surface Segregation in $Ni_xMg_{1-x}O(100)$ Solid Solutions from First Principles Calculations. *Catal. Lett.* **2012**, *142*, 1211.

(15) Pacchioni, G.; Di Valentin, C.; Dominguez-Ariza, D.; Illas, F.; Bredow, T.; Klüner, T.; Staemmler, V. Bonding of NH3, CO, and NO to NiO and Ni-doped MgO: a Problem for Density Functional Theory. *J. Phys.: Condens. Matter* **2004**, *16*, S2497−S2507.

(16) Wichtendahl, R.; Rodriguez-Rodrigo, M.; Härtel, U.; Kuhlenbeck, H.; Freund, H.-J. TDS Study of the Bonding of CO and NO to Vacuum-Cleaved NiO(100). *Surf. Sci.* **1999**, *423*, 90−98.

(17) Hoeft, J. T.; Kittel, M.; Polcik, M.; Bao, S.; Toomes, R. L.; Kang, J.-H.; Woodruff, D. P.; Pascal, M.; Lamont, C. L. A. Molecular Adsorption Bond Lengths at Metal Oxide Surfaces: Failure of Current Theoretical Methods. *Phys. Rev. Lett.* **2001**, *87*, 086101.

(18) Kittel, M.; Hoeft, J. T.; Bao, S.; Polcik, M.; Toomes, R. L.; Kang, J.-H.; Woodruff, D. P.; Pascal, M.; Lamont, C. L. A. The Local Adsorption Geometry of CO and NH_3 on NiO(100) Determined by Scanned-Energy Mode Photoelectron Diffraction. *Surf. Sci.* **2002**, *499*, 1−14.

(19) Valero, R.; Gomes, J. R.; Truhlar, D. G.; Illas, F. Density Functional Study of CO and NO Adsorption on Ni-doped MgO(100). *J. Chem. Phys.* **2010**, *132*, 104701.

(20) Perdew, J. P.; Ernzerhof, M.; Burke, K. Rationale for Mixing Exact Exchange with Density Functional Approximations. *J. Chem. Phys.* **1996**, *105*, 9982−9985.

(21) Richter, N. A.; Sicolo, S.; Levchenko, S. V.; Sauer, J.; Scheffler, M. Concentration of Vacancies at Metal-Oxide Surfaces: Case Study of MgO(100). *Phys. Rev. Lett.* **2013**, *111*, 045502.

(22) Gavartin, J. L.; Sushko, P. V.; Shluger, A. L. Modeling Charge Self-trapping in Wide-gap Dielectrics: Localization Problem in Local Density Functionals. *Phys. Rev. B: Condens. Matter Mater. Phys.* **2003**, *67*, 035108.

(23) Hofmann, O. T.; Atalla, V.; Moll, N.; Rinke, P.; Scheffler, M. Interface Dipoles of Organic Molecules on Ag(111) in Hybrid Density-Functional Theory. *New J. Phys.* **2013**, *15*, 123028.

(24) Moussa, J. E.; Schultz, P. A.; Chelikowsky, J. R. Analysis of the Heyd-Scuseria-Ernzerhof Density Functional Parameter Space. *J. Chem. Phys.* **2012**, *136*, 204117.

DOI: 10.1021/acs.jpcc.6b09505
J. Phys. Chem. C 2016, 120, 26934−26944

(25) Heyd, J.; Scuseria, G. E.; Ernzerhof, M. Hybrid Functionals Based on a Screened Coulomb Potential. *J. Chem. Phys.* **2003**, *118*, 8207−8215.
(26) Krukau, A. V.; Vydrov, O. A.; Izmaylov, A. F.; Scuseria, G. E. Influence of the Exchange Screening Parameter on the Performance of Screened Hybrid Functionals. *J. Chem. Phys.* **2006**, *125*, 224106.
(27) Neese, F. The ORCA Program System. *WIREs Comput. Mol. Sci.* **2012**, *2*, 73−78.
(28) Blum, V.; Gehrke, R.; Hanke, F.; Havu, P.; Havu, V.; Ren, X.; Reuter, K.; Scheffler, M. Ab initio Molecular Simulations with Numeric Atom-Centered Orbitals. *Comput. Phys. Commun.* **2009**, *180*, 2175−2196.
(29) Jurečka, P.; Hobza, P. On the Convergence of the $(\Delta E^{CCSD(T)}-\Delta E^{MP2})$ Term for Complexes with Multiple H-bonds. *Chem. Phys. Lett.* **2002**, *365*, 89−94.
(30) Dunning, T. H., Jr. Gaussian Basis Sets for Use in Correlated Molecular Calculations. I. The Atoms Boron Through Neon and Hydrogen. *J. Chem. Phys.* **1989**, *90*, 1007−1023.
(31) Zhang, I. Y.; Ren, X.; Rinke, P.; Blum, V.; Scheffler, M. Numeric Atom-Centered-Orbital Basis Sets with Valence-Correlation Consistency from H to Ar. *New J. Phys.* **2013**, *15*, 123033.
(32) van Lenthe, E.; Baerends, E.; Snijders, J. Relativistic Regular Two-Component Hamiltonians. *J. Chem. Phys.* **1993**, *99*, 4597.
(33) Levchenko, S. V.; Ren, X.; Wieferink, J.; Johanni, R.; Rinke, P.; Blum, V.; Scheffler, M. Hybrid Functionals for Large Periodic Systems in an All-Electron, Numeric Atom-Centered Basis Framework. *Comput. Phys. Commun.* **2015**, *192*, 60−69.
(34) Tkatchenko, A.; DiStasio, R. A., Jr.; Car, R.; Scheffler, M. Accurate and Efficient Method for Many-Body van der Waals Interactions. *Phys. Rev. Lett.* **2012**, *108*, 236402.
(35) Vegard, L. Die Konstitution der Mischkristalle und die Raumfüllung der Atome. *Eur. Phys. J. A* **1921**, *5*, 17−26.
(36) Scheffler, M. Lattice Relaxations at Substitutional Impurities in Semiconductors. *Physica B+C (Amsterdam)* **1987**, *146*, 176−186.
(37) Tanaka, S. Cohesive Energy of NiO: a Quantum Monte Carlo Approach. *J. Phys. Soc. Jpn.* **1993**, *62*, 2112−2119.
(38) *Handbook of Chemistry and Physics*; Weast, R. C., Ed.; CRC Press: Boca Raton, FL, 1987.
(39) Fuchs, M.; Niquet, Y.-M.; Gonze, X.; Burke, K. Describing Static Correlation in Bond Dissociation by Kohn−Sham Density Functional Theory. *J. Chem. Phys.* **2005**, *122*, 094116.
(40) Slater, J. C.; Wood, J. H. Statistical Exchange and the Total Energy of a Crystal. *Int. J. Quantum Chem.* **1970**, *5*, 3−34.
(41) Janak, J. F. Proof that $\partial E/\partial n_i = \varepsilon$ in Density-Functional Theory. *Phys. Rev. B: Condens. Matter Mater. Phys.* **1978**, *18*, 7165−7168.
(42) Mehdaoui, I.; Klüner, T. Bonding of CO and NO to NiO(100): a Strategy for Obtaining Accurate Adsorption Energies. *J. Phys. Chem. A* **2007**, *111*, 13233−13237.
(43) Jensen, M. B.; Pettersson, L. G. M.; Swang, O.; Olsbye, U. CO_2 Sorption on MgO and CaO Surfaces: A Comparative Quantum Chemical Cluster Study. *J. Phys. Chem. B* **2005**, *109*, 16774−16781.
(44) Ren, X.; Rinke, P.; Joas, C.; Scheffler, M. Random-Phase Approximation and its Applications in Computational Chemistry and Materials Science. *J. Mater. Sci.* **2012**, *47*, 7447−7471.
(45) Tait, S.; Dohnálek, Z.; Campbell, C. T.; Kay, B. D. n-Alkanes on MgO(100) II. Chain Length Dependence of Kinetic Desorption Parameters for Small n-Alkane. *J. Chem. Phys.* **2005**, *122*, 164708.
(46) Jung, D. R.; Cui, J.; Frankl, D. R. Dynamics and Kinetics of Monolayer CH_4 on MgO(001) Studied by Helium-Atom Scattering. *Phys. Rev. B: Condens. Matter Mater. Phys.* **1991**, *43*, 10042−10050.
(47) Tosoni, S.; Sauer, J. Accurate Quantum Chemical Energies for the Interaction of Hydrocarbons with Oxide Surfaces: CH_4/MgO-(001). *Phys. Chem. Chem. Phys.* **2010**, *12*, 14330−14340.
(48) Hu, C.-W.; Yang, H.-Q.; Wong, N.-B.; Chen, Y.-Q.; Gong, M.-C.; Tian, A.-M.; Li, C.; Li, W.-K. Theoretical Study on the Mechanism of the Reaction of CH_4 + MgO. *J. Phys. Chem. A* **2003**, *107*, 2316−2323.
(49) Ferrari, A. M.; Huber, S.; Knözinger, H.; Neyman, K. M.; Rösch, N. FTIR Spectroscopic and Density Functional Model Cluster Studies of Methane Adsorption on MgO. *J. Phys. Chem. B* **1998**, *102*, 4548−4555.
(50) Drummond, M. L.; Sumpter, B. G.; Shelton, W. A., Jr.; Larese, J. Z. Electronic Structure Investigation of Surface−Adsorbate and Adsorbate−Adsorbate Interactions in Multilayers of CH_4 on MgO(100). *J. Phys. Chem. C* **2007**, *111*, 966−976.
(51) Kwapien, K.; Sierka, M.; Döbler, J.; Sauer, J. Reactions of H_2, CH_4, C_2H_6 and C_3H_8 with $[(MgO)_n]^+$ Clusters Studied by Density Functional Theory. *ChemCatChem* **2010**, *2*, 819−826.
(52) Ito, T.; Tashiro, T.; Watanabe, T.; Toi, K.; Ikemoto, I. Activation of Methane on the MgO Surface at Low Temperatures. *Chem. Lett.* **1987**, *16*, 1723−1726.
(53) Liu, Z.; Grinter, D. C.; Lustemberg, P. G.; Nguyen-Phan, T.-D.; Zhou, Y.; Luo, S.; Waluyo, I.; Crumlin, E. J.; Stacchiola, D. J.; Zhou, J.; et al. Dry Reforming of Methane on a Highly-Active Ni-CeO_2 Catalyst: Effects of Metal-Support Interactions on C-H Bond Breaking. *Angew. Chem., Int. Ed.* **2016**, *55*, 7455−7459.
(54) Cornu, D.; Guesmi, H.; Krafft, J.-M.; Lauron-Pernot, H. Lewis Acido-Basic Interactions between CO_2 and MgO Surface: DFT and DRIFT Approaches. *J. Phys. Chem. C* **2012**, *116*, 6645−6654.
(55) Pacchioni, G. Physisorbed and Chemisorbed CO_2 at Surface and Step Sites of the MgO(l00) Surface. *Surf. Sci.* **1993**, *281*, 207−219.
(56) Downing, C. A.; Sokol, A. A.; Catlow, C. R. A. The Reactivity of CO_2 on the MgO(100) Surface. *Phys. Chem. Chem. Phys.* **2014**, *16*, 184−195.
(57) Baltrusaitis, J.; Hatch, C.; Orlando, R. Periodic DFT Study of Acidic Trace Atmospheric Gas Molecule Adsorption on Ca- and Fe-Doped MgO(001) Surface Basic Sites. *J. Phys. Chem. A* **2012**, *116*, 7950−7958.
(58) Meixner, D.; Arthur, D.; George, S. Kinetics of Desorption, Adsorption and Surface Diffusion of CO_2 on MgO(100). *Surf. Sci.* **1992**, *261*, 141−154.
(59) Wichtendahl, R.; Rodriguez-Rodrigo, M.; Härtel, U.; Kuhlenbeck, H.; Freund, H.-J. Thermodesorption of CO and NO from Vacuum-Cleaved NiO(100) and MgO(100). *Phys. Status Solidi A* **1999**, *173*, 93−100.
(60) Staemmler, V. Method of Local Increments for the Calculation of Adsorption Energies of Atoms and Small Molecules on Solid Surfaces. 2. CO/MgO(001). *J. Phys. Chem. A* **2011**, *115*, 7153−7160.
(61) Boese, A. D.; Sauer, J. Accurate Adsorption Energies of Small Molecules on Oxide Surfaces: CO−MgO(001). *Phys. Chem. Chem. Phys.* **2013**, *15*, 16481−16493.
(62) Dohnálek, Z.; Kimmel, G. A.; Joyce, S. A.; Ayotte, P.; Smith, R. S.; Kay, B. D. Physisorption of CO on the MgO(100) Surface. *J. Phys. Chem. B* **2001**, *105*, 3747−3751.
(63) Freund, H.-J. Adsorption of Gases on Complex Solid Surfaces. *Angew. Chem., Int. Ed. Engl.* **1997**, *36*, 452−475.
(64) Shluger, A. L.; Gale, J. D.; Catlow, C. R. A. Molecular Properties of the Magnesia Surface. *J. Phys. Chem.* **1992**, *96*, 10389−10397.
(65) Anchell, J. L.; Morokuma, K.; Hess, A. C. An Electronic Structure Study of H_2 and CH_4 Interactions with MgO and Li-doped MgO Clusters. *J. Chem. Phys.* **1993**, *99*, 6004.
(66) Kobayashi, H.; Salahub, D. R.; Ito, T. Dissociative Adsorption of Hydrogen Molecule on MgO Surfaces Studied by the Density Functional Method. *J. Phys. Chem.* **1994**, *98*, 5487−5492.
(67) Chen, H.-Y. T.; Giordano, L.; Pacchioni, G. From Heterolytic to Homolytic H_2 Dissociation on Nanostructured MgO(001) Films As a Function of the Metal Support. *J. Phys. Chem. C* **2013**, *117*, 10623−10629.

DOI: 10.1021/acs.jpcc.6b09505
J. Phys. Chem. C 2016, 120, 26934−26944